CHAPTER FOUR

Optical image processing using photonic crystal slab

Cheng Guo[a], Shanhui Fan[b,*]
[a]Department of Applied Physics, Stanford University, Stanford, CA, United States
[b]Ginzton Laboratory and Department of Electrical Engineering, Stanford University, Stanford, CA, United States
*Corresponding author: e-mail address: shanhui@stanford.edu

Contents

1. Introduction

In this chapter we will discuss the use of photonic crystal slab to accomplish a number of imaging processing tasks, including edge detection, image smoothing, white noise suppression, and suppression or extraction of periodic features. All these tasks involve filtering in the wavevector domain. These tasks are of broad applications ranging from microscopy and medical imaging to industrial inspection and object detection (Abràmoff et al., 2004; Brosnan and Sun, 2004; Dalal and Triggs, 2005; Gonzalez and Woods, 2008; Markham et al., 1963).

All these image processing operations, as mentioned above, can certainly be implemented using conventional electronic computing. However, nowadays there are many big-data applications that require real-time and high-throughput image processing, for which it is of interest to develop

techniques to perform these computations with reduced energy consumption and increased speed. Optical image processing is particularly suitable for this purpose, since the images are naturally in the optical domain. Moreover, many of these tasks can be achieved using linear optical devices that have no power consumption except the propagation loss of light through the device, and have very low latency since the latency is determined only by the time for light to propagate through these devices.

Traditionally, optical image processing can be performed using the techniques of Fourier optics. For instance, to achieve filtering in the wavevector domain, one first obtains a Fourier transformation of an image on a Fourier plane by passing the image through a lens. One then performs a spatial filtering on the Fourier plane, followed by a Fourier transformation again through a second lens (Goodman, 2005; Yu et al., 2001). Such technique requires long propagation distance and therefore results in a bulky system (Chang et al., 1990; Eu et al., 1973; Görlitz and Lanzl, 1975; Sirohi and Mohan, 1977).

Thanks to the recent progress in nanophotonics, optical image processing can instead be achieved by compact photonic devices (AbdollahRamezani et al., 2015; Bykov et al., 2014, 2018; Chizari et al., 2016; Dong et al., 2018; Fang and Ruan, 2018; Fang et al., 2017; Golovastikov et al., 2014; Guo et al., 2018b; Hwang et al., 2018; Kwon et al., 2018; Nejad and Fleury, 2018; Pors et al., 2015; Roberts et al., 2018; Silva et al., 2014; Solli and Jalali, 2015; Wu et al., 2017; Youssefi et al., 2016; Zhu et al., 2017). In this chapter, we provide a brief review of optical image processing using the guided resonance in a two-dimensional photonic crystal slab device. In particular, we focus on a particular class of photonic crystal slab structure where the guided resonance near the Γ point exhibits an isotropic band structure. Depending on the light frequency and the choice of transmission or reflection mode, this compact device realizes high-pass, low-pass, band-reject, and band-pass filtering directly in the optical domain. These filtering operations are applied isotropically in the two-dimensional plane, which is particularly attractive for image processing.

The rest of this chapter is organized as follows. In Section 2 we elucidate the underlying physics mechanism of filtering in the wavevector domain using guided resonances. This mechanism underlies the operation of many compact nanophotonic devices for image filtering, including ours. In Section 3 we theoretically analyze how to realize isotropic filters by a photonic crystal slab device using guided resonances with carefully designed isotropic band structures. In Section 4 we numerically demonstrate the isotropic filtering functions of the device. We conclude in Section 5.

2. Filtering in the wavevector domain using guided resonances

We consider a filter in the wavevector domain as characterized by the filter transfer function $H(k_x, k_y)$ (Bracewell, 1986). In general, for a near-normally incident light beam along the z axis with a transverse field profile $S_{in}(x, y)$, upon the operation of the filter, the output beam has a profile $S_{out}(x, y) = \mathcal{F}^{-1}[H(k_x, k_y)\widetilde{S}_{in}(k_x, k_y)]$, where $\mathcal{F}^{-1}$ denotes the inverse Fourier transform and $\widetilde{S}_{in}(k_x, k_y)$ is the Fourier transform of the input image (Gonzalez and Woods, 2008). If $H(k_x, k_y) = H(|\boldsymbol{k}|)$, i.e., H only depends on the magnitude of the wavevector $|\boldsymbol{k}|$, the filter is isotropic. Here $\boldsymbol{k} = (k_x, k_y)$ refers to the in-plane wavevector.

Filtering in the wavevector domain can be realized using guided resonances hosted by compact photonic device. In general, guided resonances can induce sharp Fano resonance features in the transmission and reflection spectra (Fan and Joannopoulos, 2002; Ochiai and Sakoda, 2001; Tikhodeev et al., 2002; Zhou et al., 2014). Since the band structures of the guided resonances are usually dispersive, i.e., the resonant frequency is wavevector dependent, the transmission and reflection spectra are also wavevector dependent. Filtering in the wavevector domain can thus be realized in both transmission and reflection modes at a specific frequency.

As an illustration, we first show how to use guided resonances to realize second-order differentiation, a specific type of high-pass filter, at transmission along the direction normal to the slab (Guo et al., 2018b). The task is to design an optical system with a transfer function in the wavevector space ($\boldsymbol{k}$-space) of the form $t(\boldsymbol{k}) = \alpha|\boldsymbol{k}|^2$. For one-dimensional differentiation, $\boldsymbol{k} = k_x$; for two-dimensional differentiation, $\boldsymbol{k} = (k_x, k_y)$. We consider the transmission coefficient of a photonic structure which supports a single band of guided resonances as characterized by $\boldsymbol{k}$-dependent resonant frequencies $\omega(\boldsymbol{k})$ and radiative linewidths $\gamma(\boldsymbol{k})$ (Fig. 1A). Near the resonant frequencies, the transmitted amplitude t is expressed as (Fan and Joannopoulos, 2002)

$$t(\omega, \boldsymbol{k}) = t_d + f\frac{\gamma(\boldsymbol{k})}{i[\omega - \omega(\boldsymbol{k})] + \gamma(\boldsymbol{k})}, \tag{1}$$

where ω is the incident light frequency, t_d is the direct transmission coefficient, and f is related to the complex decaying amplitude of the resonance to the transmission side of the slab.
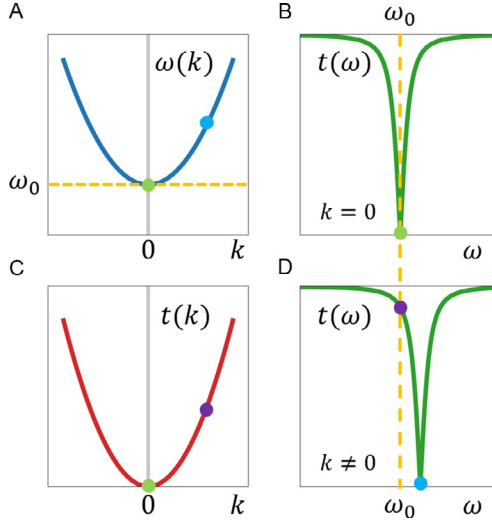
Fig. 1 Operating principle of filtering in the wavevector domain using guided resonances. (A) Dispersion for a single band of guided resonance $\omega(k)$. (B) Transmission spectrum $t(\omega)$ at $k = 0$. (C) k-dependent transmission coefficient $t(k)$ at the resonant frequency at $k = 0$: $\omega = \omega_0$. (D) Transmission spectrum $t(\omega)$ at $k \neq 0$.

In general, f is constrained by the direct process if the system satisfies energy conservation and time-reversal symmetry (Fan and Joannopoulos, 2002; Wang et al., 2013). In particular, if $t_d = 1$, that is, the direct pathway has a 100% transmission coefficient, then

$$f = -t_d = -1 \tag{2}$$

as has been derived in Wang et al. (2013). In this special case,

$$t(\omega, \boldsymbol{k}) = 1 - \frac{\gamma(\boldsymbol{k})}{i[\omega - \omega(\boldsymbol{k})] + \gamma(\boldsymbol{k})}. \tag{3}$$

We plot the spectra of transmission coefficient amplitude $t(\omega)$ at $k = 0$ and $k \neq 0$ in Fig. 1B and D, respectively. Using Eq. (3), zero transmission occurs at the $\boldsymbol{k}$-dependent resonant frequency:

$$\omega = \omega(\boldsymbol{k}). \tag{4}$$

We denote $\omega_0 = \omega(\boldsymbol{k} = \boldsymbol{0})$ and $\gamma_0 = \gamma(\boldsymbol{k} = \boldsymbol{0})$. If we fix the frequency $\omega = \omega_0$, the transmission coefficient $t(\omega_0, \boldsymbol{k})$ is then $\boldsymbol{k}$-dependent. We can perform an expansion of t near $\boldsymbol{k} = \boldsymbol{0}$:

$$t(\omega_0, \boldsymbol{k}) = 0 + \frac{\partial t}{\partial \omega(\boldsymbol{k})}\bigg|_{\Gamma} \delta\omega(\boldsymbol{k}) + \frac{\partial t}{\partial \gamma(\boldsymbol{k})}\bigg|_{\Gamma} \delta\gamma(\boldsymbol{k}), \tag{5}$$

where

$$\delta\omega(\boldsymbol{k}) = \omega(\boldsymbol{k}) - \omega_0, \quad \delta\gamma(\boldsymbol{k}) = \gamma(\boldsymbol{k}) - \gamma_0, \tag{6}$$

$$\frac{\partial t}{\partial \omega(\boldsymbol{k})}\bigg|_{\Gamma} = -\frac{i}{\gamma_0}, \quad \frac{\partial t}{\partial \gamma(\boldsymbol{k})}\bigg|_{\Gamma} = 0, \tag{7}$$

therefore,

$$t(\omega_0, \boldsymbol{k}) = -\frac{i}{\gamma_0}\delta\omega(\boldsymbol{k}). \tag{8}$$

In this special case, $t(\boldsymbol{k})$ is simply proportional to the band dispersion $\delta\omega(\boldsymbol{k})$ near $\boldsymbol{k} = \boldsymbol{0}$. If $\delta\omega(\boldsymbol{k}) \propto |\boldsymbol{k}|^2$, then $t(\boldsymbol{k}) \propto |\boldsymbol{k}|^2$ as well.

The analysis above indicates that to use guided resonances to perform second-order differentiation, it is sufficient to satisfy the following three conditions:

1. $t_d = 1$.
2. Only one guided resonance band is coupled.
3. The band satisfies the dispersion $(\omega(\boldsymbol{k}) - \omega_0) \propto |\boldsymbol{k}|^2$.

While the discussion above is specific to differentiation, it is relevant for understanding of some of the other filter functionalities as well. Based on the discussion here, in the next section we will illustrate how to use a photonic crystal slab to achieve these filter functionalities.

3. Theoretical analysis of isotropic filters using a photonic crystal slab

In this section, based on the discussion above, we theoretically analyze how to realize isotropic filters using a photonic crystal slab device. Depending on the light frequency and the choice of transmission or reflection mode, this compact device realizes isotropic high-pass, low-pass, band-reject, and band-pass filtering directly in the optical domain (Guo et al., 2018a).

The device is shown in Fig. 2. The dielectric constant of the material for the slabs is $\epsilon = 4.67$, which approximates that of Si_3N_4 in the visible wavelength range. Here we use a dielectric constant that is real, as the extinction coefficient of Si_3N_4 at visible wavelength is negligible. The photonic crystal slab has a thickness of $d = 0.50a$ and a square lattice of air holes with
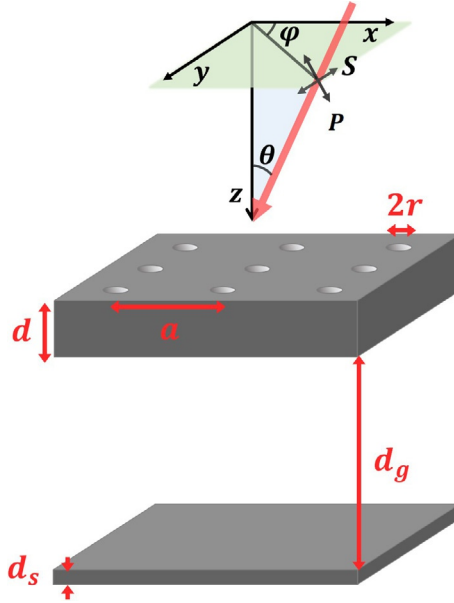
Fig. 2 Geometry of the device, which consists of a photonic crystal slab with a square lattice of air holes, separated from a uniform dielectric slab by an air gap. The slabs have a dielectric constant $\epsilon = 4.67$. The geometry parameters are: $d = 0.50a$, $r = 0.11a$, $d_s = 0.12a$, $d_g = 1.93a$, where a is the lattice constant. The coordinate system is shown above the device. The *red arrow* indicates the direction of the incident light. The electric field directions of the S and P-polarized light are also indicated. *Reprinted with permission from Guo, C., Xiao, M., Minkov, M., Shi, Y., Fan, S., 2018a. Isotropic wavevector domain image filters by a photonic crystal slab device. J. Opt. Soc. Am. A Opt. Image Sci. Vis. 35 (10), 1685–1691, the Optical Society.*

radii $r = 0.11a$, where a is the lattice constant. The thickness d and radius r are chosen to realize isotropic bands of guided resonances. A uniform dielectric slab with a thickness $d_s = 0.12a$ is placed in the vicinity of the photonic crystal slab. The air gap between the two slabs has a thickness $d_g = 1.93a$. As a side note, the two–layer structure we use in the chapter is quite compact. For a resonant wavelength $\lambda = 500$ nm and $a = 650$ nm the total thickness is $d + d_g + d_s = 1.66 \, \mu$m. Such structure can be fabricated using focused ion beam–assisted laser interference lithography (Vogelaar et al., 2001).

To satisfy the first criterion in Section 2, we note that the direct transmission coefficient t_d is related to the nonresonant transmission pathway (Ochiai and Sakoda, 2001). Hence, it is possible to realize $t_d = 1$ by changing the thickness of the slab. In the structure as shown in Fig. 2, we achieve $t_d = 1$ by placing a uniform dielectric slab in the vicinity of the photon crystal

slab, and by tuning the distance between the slabs. This has the advantage that we can tune t_d without significantly affecting the band structure of the photonic crystal slab.

To satisfy the second and third criterion in Section 2, one will need to design the band structure of the guided resonances. The design here is in fact quite nontrivial due to the vectorial nature of electromagnetic waves. Since the required filter transfer function $H(\mathbf{k})$ is isotropic in $\mathbf{k}$-space, it is natural to consider a photonic crystal slab structure that possesses rotational symmetry. As an illustration, here we consider a slab structure with a square lattice of air holes that has C_{4v} symmetry. For concreteness, we consider circular holes; the same analysis will apply to other hole shapes that preserve C_{4v} symmetry. For such a slab, it is known that at the Γ point, which corresponds to $|\mathbf{k}| = 0$, the only modes that can couple to external plane waves must be twofold degenerate, belonging to the two-dimensional irreducible representation of the C_{4v} group (Fan and Joannopoulos, 2002; Ochiai and Sakoda, 2001). Near such modes, in the vicinity of the Γ point, from the $\mathbf{k} \cdot \mathbf{p}$ analysis, the band structure in general can be described by the following 2×2 effective Hamiltonian. (As we consider only small wavevector range near the Γ point, it is sufficient to include only the two modes at the Γ point in our $\mathbf{k} \cdot \mathbf{p}$ analysis.)

$$\hat{\mathcal{H}}(\mathbf{k}) = (\omega_0 - i\gamma_0 + a|\mathbf{k}|^2)\hat{\mathbf{I}} + b(k_x^2 - k_y^2)\hat{\boldsymbol{\sigma}}_z + ck_xk_y\hat{\boldsymbol{\sigma}}_x, \tag{9}$$

where a, b, c are three complex coefficients and the $\boldsymbol{\sigma}$'s are the Pauli matrices. This Hamiltonian has two eigenvalues of

$$\omega_{\pm}(\mathbf{k}) - i\gamma_{\pm}(\mathbf{k}) = \omega_0 - i\gamma_0 + a|\mathbf{k}|^2 \pm \sqrt{b^2|\mathbf{k}|^4 + (c^2 - 4b^2)k_x^2k_y^2}. \tag{10}$$

For a general choice of parameters b and c, the band structure as described by Eq. (10) is not isotropic. On the other hand, Eq. (10) also indicates that when $c = \pm 2b$, both bands will be isotropic:

$$\omega_{\pm}(\mathbf{k}) - i\gamma_{\pm}(\mathbf{k}) = \omega_0 - i\gamma_0 + (a \pm b)|\mathbf{k}|^2. \tag{11}$$

To achieve such an isotropic band structure requires detailed tuning of the parameters. Remarkably, with the carefully tuned geometry parameters as above, both bands of the guided resonances that are degenerate at Γ with a frequency $\omega_0 = 0.77098 \times 2\pi c/a$ exhibit almost complete circular symmetry in the real part of the eigenfrequencies:

$$\omega_{\pm}(\mathbf{k}) \approx \omega_0 + A_{\pm}|\mathbf{k}|^2, \tag{12}$$

where $A_+ = 4.35$, $A_- = -1.41$, and the upper (lower) sign corresponds to the upper (lower) band. In Eq. (12), and throughout the rest of the chapter, the wavevector will be in the unit of $2\pi/a$.

The nearly isotropic photonic band structure $(\omega_\pm(\mathbf{k}) - \omega_0)$ for the structure shown in Fig. 2 is plotted in Fig. 3A, C, and D. Fig. 3A shows that for both bands, the dispersions along the Γ–M and Γ–X directions have almost identical effective masses. Here the effective mass tensor is defined as $m_{ij}^* = \hbar[\partial^2 \omega(\mathbf{k})/\partial k_i \partial k_j]^{-1}$. Fig. 3C and D shows that the constant frequency contours for both bands are almost circular. We note that the radiative linewidths $\gamma_\pm(\mathbf{k})$, unlike $\omega_\pm(\mathbf{k})$, are anisotropic. Nonetheless, $(\gamma_\pm(\mathbf{k}) - \gamma_0)$ are much smaller than $(\omega_\pm(\mathbf{k}) - \omega_0)$, thus do not affect the circular symmetry of the transfer functions much, as we will show later.

As we mentioned above, for a structure with C_{4v} symmetry, the modes that a normally incident plane wave can couple to at the Γ point are always two-fold degenerate. Consequently, near the Γ point, there are always two bands of guided resonances present. Moreover, off the normal direction, if the direction of incident waves is away from the high symmetry planes, both S and P polarized lights may couple to both bands, leading to complicated polarization conversion effects. Thus, in general, in addition to having an anisotropic band structure near Γ, a photonic crystal slab structure also does not satisfy the criterion 2 above in Section 2 regarding the excitation of a single guided resonance band. Remarkably, however, below we show that once the condition for isotropic bands is satisfied, each of the two bands in fact only couples to one single polarization, *for every direction of incidence*. Below, we refer to this effect, where each polarization excites only a single band away from normal incidence, as the effect of *single-band excitation*. Due to the single-band excitation effect, S and P polarizations are decoupled in this special case.

To illustrate the effect of single-band excitation for every direction when the bands are isotropic, we first show that single-band excitation always occurs when the incident direction is in a mirror symmetry plane of the structure. Using the group theory notation in Sakoda (2005), as our system possesses C_{4v} symmetry, the doubly degenerate states at Γ are E modes. Along the Γ–X direction, this pair of E modes splits into two singly degenerate states of A and B modes which are even and odd, respectively, with respect to the reflection operator associated with the mirror plane $y = 0$. On the other hand, since the S and P polarized lights are odd and even with respect to the same mirror plane, respectively, along the Γ–X direction, the $S(P)$ polarized light can only couple to the $B(A)$ mode. Thus, in general, we
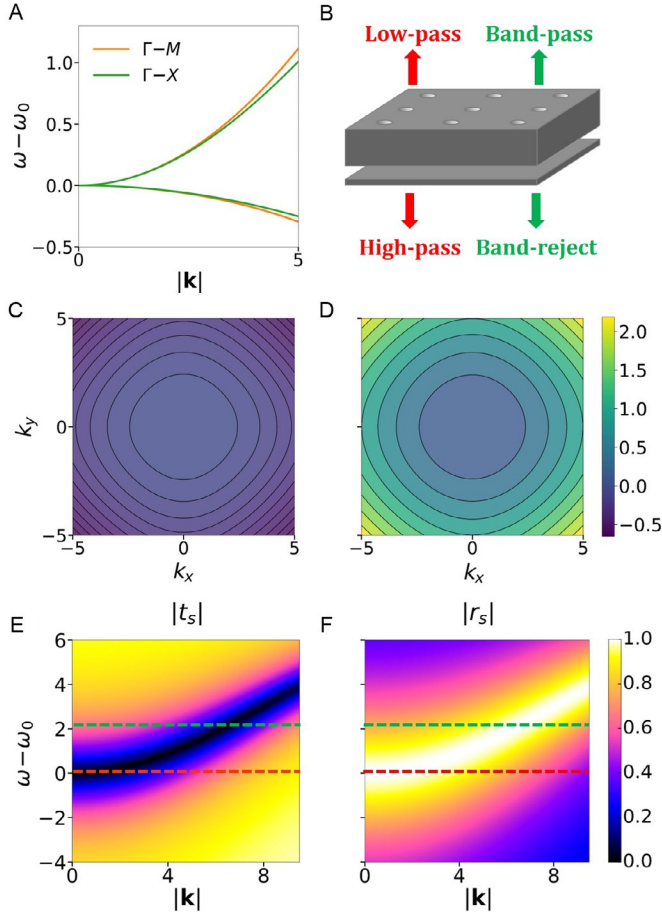
Fig. 3 (A, C, D) Nearly isotropic photonic band structure of the photonic crystal slab shown in Fig. 1 near the frequency $\omega_0 = 0.77098 \times 2\pi c/a$. (A) Band dispersions along Γ–X and Γ–M directions. (C) Constant frequency contours of the lower band. (D) Constant frequency contours of the upper band. (B) Scheme of multiple filtering functions of the device. When the light frequency is on resonance at the normal incidence ($\omega = \omega_0$, labeled by *red arrows* in (B) and *red horizontal lines* in (E,F)), the device realizes isotropic high-pass filter (Laplacian) at transmission and low-pass filter at reflection. When the light frequency is detuned from the resonance at the normal incidence ($\omega = \omega_k$, labeled by *green arrows* in (B) and *green horizontal lines* in (E,F)), the device realizes isotropic band-reject filter at transmission and band-pass filter at reflection. (E) Transmittance $|t|$ for S polarized light as a function of ω and $|k|$ near $\omega_0 = 0.77098 \times 2\pi c/a$ along a general wavevector direction ($\varphi = 14°$). Due to the isotropic band structure, S light only excites the upper band, and the transmission spectra are almost identical along any wavevector direction φ. $|t| = 0$ when $\omega = \omega(k)$. (F) Reflectance $|r|$ for S polarized light as a function of ω and $|k|$ near $\omega_0 = 0.77098 \times 2\pi c/a$ along a general wavevector direction ($\varphi = 14°$). The reflection spectra are identical along any wavevector direction. $|r| = 1$ when $\omega = \omega(k)$. In all the plots, frequency ($\omega - \omega_0$) is in the units of $10^{-4} \times 2\pi c/a$, while $|k|$, k_x, and k_y are in the units of $10^{-3} \times 2\pi/a$. *Reprinted with permission from Guo, C., Xiao, M., Minkov, M., Shi, Y., Fan, S., 2018a. Isotropic wavevector domain image filters by a photonic crystal slab device. J. Opt. Soc. Am. A Opt. Image Sci. Vis. 35 (10), 1685–1691, the Optical Society.*

have the effect of single-band excitation when the direction of incidence is in a high symmetry plane such as the $\gamma = 0$ plane (Tikhodeev et al., 2002).

Next, we prove the following statement: if the two-band Hamiltonian is isotropic, that is,

$$\hat{\mathcal{R}}(\varphi)\hat{\mathcal{H}}(\boldsymbol{k})\hat{\mathcal{R}}^{-1}(\varphi) = \hat{\mathcal{H}}(\boldsymbol{R}(\varphi)\boldsymbol{k}), \tag{13}$$

for every $\varphi \in (0, 2\pi)$, then we have the effect of single-band excitation along all directions. Here, $\boldsymbol{R}(\varphi)$ and $\hat{\mathcal{R}}(\varphi)$ are the rotation operators that describe the rotation around the z-axis by an angle φ, in the $\boldsymbol{k}$ space and the two-dimensional Hilbert space, respectively. To prove this, we denote the eigenstates of the two bands as $|\boldsymbol{k}, A\rangle$ and $|\boldsymbol{k}, B\rangle$, which connect to the A and B modes along the Γ-X direction, respectively. Eq. (13) implies that:

$$\begin{aligned} |\boldsymbol{R}(\varphi)\boldsymbol{k}, A\rangle &= \hat{\mathcal{R}}(\varphi)|\boldsymbol{k}, A\rangle, \\ |\boldsymbol{R}(\varphi)\boldsymbol{k}, B\rangle &= \hat{\mathcal{R}}(\varphi)|\boldsymbol{k}, B\rangle. \end{aligned} \tag{14}$$

We denote the S and P polarized modes as $|\boldsymbol{k}, S\rangle$ and $|\boldsymbol{k}, P\rangle$, respectively. By definition,

$$\begin{aligned} |\boldsymbol{R}(\varphi)\boldsymbol{k}, S\rangle &= \hat{\mathcal{R}}(\varphi)|\boldsymbol{k}, S\rangle, \\ |\boldsymbol{R}(\varphi)\boldsymbol{k}, P\rangle &= \hat{\mathcal{R}}(\varphi)|\boldsymbol{k}, P\rangle. \end{aligned} \tag{15}$$

For $\boldsymbol{k} = \boldsymbol{k_x}$ along the $\Gamma-X$ direction, the $A(B)$ mode does not couple to the $S(P)$ polarization, i.e.,

$$\begin{aligned} \langle \boldsymbol{k_x}, S|\boldsymbol{k_x}, A\rangle &= 0, \\ \langle \boldsymbol{k_x}, P|\boldsymbol{k_x}, B\rangle &= 0. \end{aligned} \tag{16}$$

Then for $\boldsymbol{k} = \boldsymbol{R}(\varphi)\boldsymbol{k_x}$ along any direction, using Eqs. (14) and (15), we also have

$$\begin{aligned} \langle \boldsymbol{k}, S|\boldsymbol{k}, A\rangle &= \langle \boldsymbol{k_x}, S|\hat{\mathcal{R}}^{-1}(\varphi)\hat{\mathcal{R}}(\varphi)|\boldsymbol{k_x}, A\rangle = 0, \\ \langle \boldsymbol{k}, P|\boldsymbol{k}, B\rangle &= \langle \boldsymbol{k_x}, P|\hat{\mathcal{R}}^{-1}(\varphi)\hat{\mathcal{R}}(\varphi)|\boldsymbol{k_x}, B\rangle = 0. \end{aligned} \tag{17}$$

Due to the single-band excitation effect, as well as the presence of the uniform dielectric slab which sets the background transmission coefficient (Fan and Joannopoulos, 2002) to be unity, for this structure shown in Fig. 2, the transmission and reflection coefficients are:

$$t_{\pm}(\omega, \boldsymbol{k}) = \frac{i[\omega - \omega_{\pm}(\boldsymbol{k})]}{i[\omega - \omega_{\pm}(\boldsymbol{k})] + \gamma_{\pm}(\boldsymbol{k})}, \tag{18}$$

$$r_{\pm}(\omega, \mathbf{k}) = -\mathrm{e}^{i\phi} \frac{\gamma_{\pm}(\mathbf{k})}{i[\omega - \omega_{\pm}(\mathbf{k})] + \gamma_{\pm}(\mathbf{k})}, \tag{19}$$

where the upper (lower) sign corresponds to $S(P)$ polarized light and upper (lower) band; ω is the incident light frequency. Therefore on resonance,

$$t_{\pm}(\omega_{\pm}(\mathbf{k}), \mathbf{k}) = 0, \quad r_{\pm}(\omega_{\pm}(\mathbf{k}), \mathbf{k}) = -\mathrm{e}^{i\phi}. \tag{20}$$

The numerically determined transmission and reflection spectra for S polarized light are plotted in Fig. 3E and F. Due to the effect of single-band excitation, S-polarized light only excites the upper band of guided resonances. Moreover, as expected from Eqs. (12), (18), and (19), the resultant transmission and reflection spectra are isotropic, i.e., the spectra are identical along any wavevector direction as defined by the angle φ in Fig. 2. When $\omega = \omega(\mathbf{k})$, the transmittance exhibits sharp dips with $|t| = 0$, while the reflectance exhibits peaks with $|r| = 1$, as expected from Eq. (20).

Depending on the operating conditions, the structure as shown in Fig. 2 can be used to perform several very useful image-processing functionalities (Guo et al., 2018a):

1. *Isotropic high-pass filter*

   At the frequency $\omega = \omega_0 \equiv \omega_{\pm}(k = 0)$, the $\mathbf{k}$-dependent transmittance is:

$$\begin{aligned} |t_{\pm}(\omega_0, \mathbf{k})| &= \frac{|\omega_{\pm}(\mathbf{k}) - \omega_0|}{\sqrt{[\omega_{\pm}(\mathbf{k}) - \omega_0]^2 + \gamma_{\pm}(\mathbf{k})^2}} \\ &\approx \frac{|\omega_{\pm}(\mathbf{k}) - \omega_0|}{\gamma_0} = \frac{A_{\pm}}{\gamma_0} |\mathbf{k}|^2. \end{aligned} \tag{21}$$

   This transmittance realizes the Laplacian, a special isotropic high-pass filter (Guo et al., 2018b).

2. *Isotropic low-pass filter*

   At the frequency $\omega = \omega_0$, if one considers instead the reflected light, the transfer function is:

$$\begin{aligned} |r_{\pm}(\omega_0, \mathbf{k})| &= \frac{1}{\sqrt{1 + [\omega_{\pm}(\mathbf{k}) - \omega_0]^2 / \gamma_{\pm}(\mathbf{k})^2}} \\ &\approx \frac{1}{\sqrt{1 + A_{\pm}^2 |\mathbf{k}|^4 / \gamma_0^2}}. \end{aligned} \tag{22}$$

   This transfer function realizes an isotropic low-pass filter with reflection peak $|r_{\pm}| = 1$ at the Γ point.

3. *Isotropic band-reject filter*

Suppose instead we operate away from the frequency ω_0, but at the frequency $\omega = \omega_{\pm,\ q}$, where q is the amplitude of a nonzero in-plane wavevector, the transfer function then becomes

$$|t_\pm(\omega_{\pm,\ q}, \boldsymbol{k})| = \frac{|\omega_\pm(\boldsymbol{k}) - \omega_{\pm,\ q}|}{\sqrt{[\omega_\pm(\boldsymbol{k}) - \omega_{\pm,\ q}]^2 + \gamma_\pm(\boldsymbol{k})^2}} \tag{23}$$

This transfer function realizes an isotropic band-reject filter, with transmission dip $|t_\pm| = 0$ at $|\boldsymbol{k}| = q$.

4. *Isotropic band-pass filter*

At the frequency $\omega = \omega_{\pm,\ q}$, the reflection has a transfer function

$$|r_\pm(\omega_q, \boldsymbol{k})| = \frac{1}{\sqrt{1 + [\omega_\pm(\boldsymbol{k}) - \omega_{\pm,\ q}]^2 / \gamma_\pm(\boldsymbol{k})^2}} \tag{24}$$

This transfer function realizes an isotropic band-pass filter, with reflection peak $|r_\pm| = 1$ at $|\boldsymbol{k}| = q$.

Therefore, our device can be used to achieve multiple filtering functions. As schematically shown in Fig. 3B, when the light frequency is on resonance at normal incidence ($\omega = \omega_0$), the device operates as an isotropic high-pass filter (Laplacian) at the transmission mode and an isotropic low-pass filter at the reflection mode. When the light frequency is detuned a bit from the resonance at normal incidence, the device operates as an isotropic band-reject filter at the transmission mode and an isotropic band-pass filter at the reflection mode, where the rejected or passed wavevector components are determined by the light frequency detuning and polarization. For transmission mode, the transmitted image is the required filtered result. For reflection mode, the reflected image is the required filtered result, which can be separated from the incident image by using a beam splitter.

4. Numerical demonstration of the isotropic filters

Now we numerically demonstrate the filtering functions of our device. In all the numerical demonstration below, the incident beam is S polarized. The transmitted image is calculated following the standard way in image processing (Gonzalez and Woods, 2008). (1) Compute the Fourier transform $\widetilde{S}_{in}(k_x, k_y)$ of the incident field profile $S_{in}(x, y)$. Note the incident image is $|S_{in}(x, y)|^2$. (2) Compute the Fourier transform of the output field

profile, $\tilde{S}_{out}(k_x, k_y) = H(k_x, k_y)\tilde{S}_{in}(k_x, k_y)$, where $H(k_x, k_y)$ is the transfer function. (3) Obtain the output field profile $S_{out}(x, y)$ by inverse Fourier transform. Calculate the output image $|S_{out}(x, y)|^2$.

4.1 Isotropic high-pass filter (the Laplacian)

Fig. 4 illustrates the isotropic high-pass filter (the Laplacian). Fig. 4A plots the filter transfer function: the transmittance for S-polarized light $|t_s|(k_x, k_y)$ at the frequency $\omega_0 = 0.77098 \times 2\pi c/a$. The transfer function is almost isotropic. Fig. 4B plots $|t_s|$ as a function of $|\mathbf{k}|$ along a general wavevector direction ($\varphi = 14°$), and the fitting result of Eq. (21). The fitting is very good for $|\mathbf{k}|$ up to $0.6 \times 10^{-2} \times 2\pi/a$. These plots confirm that the device indeed operates as an isotropic high-pass filter (the Laplacian) in this case. In Fig. 4A (and also in Fig. 5A as shown later), at larger wavevectors, the transfer function exhibits some anisotropy due to the dependency of the radiative linewidth $\gamma(\mathbf{k})$ on the direction of $\mathbf{k}$.

The Laplacian enables image sharpening and edge detection (Guo et al., 2018b). Fig. 4E shows an incident image of the Stanford emblem. Fig. 4C plots the Fourier transform of the field profile for this incident image. Fig. 4D shows the calculated Fourier spectrum for the transmitted image, which is obtained by a pointwise product of Fig. 4A and C. The low wavevector components have been filtered out. Fig. 4F is the calculated transmitted image, which contains only the edge of the incident image.

4.2 Isotropic low-pass filter

Fig. 5 illustrates the isotropic low-pass filter. Fig. 5A plots the filter transfer function: the reflectance for S-polarized light $|r_s|(k_x, k_y)$ at the frequency $\omega_0 = 0.77098 \times 2\pi c/a$. The transfer function is almost isotropic. Fig. 5B plots $|r_s|$ as a function of $|\mathbf{k}|$ along a general wavevector direction ($\varphi = 14°$), and the fitting result of Eq. (22). The fitting is almost perfect in the wavevector range as shown. These plots confirm that the device indeed operates as an isotropic low-pass filter in this case.

The isotropic low-pass filter accomplishes image smoothing, with applications ranging from character recognition in machine perception, pre-processing functions in printing and publishing industry, to satellite and aerial image processing (Buades et al., 2005; Gonzalez and Woods, 2008). Here we show one specific application of the low-pass filter in white noise reduction. Fig. 5E shows an incident image of the Stanford emblem with substantial white noise components, while Fig. 5C plots the Fourier
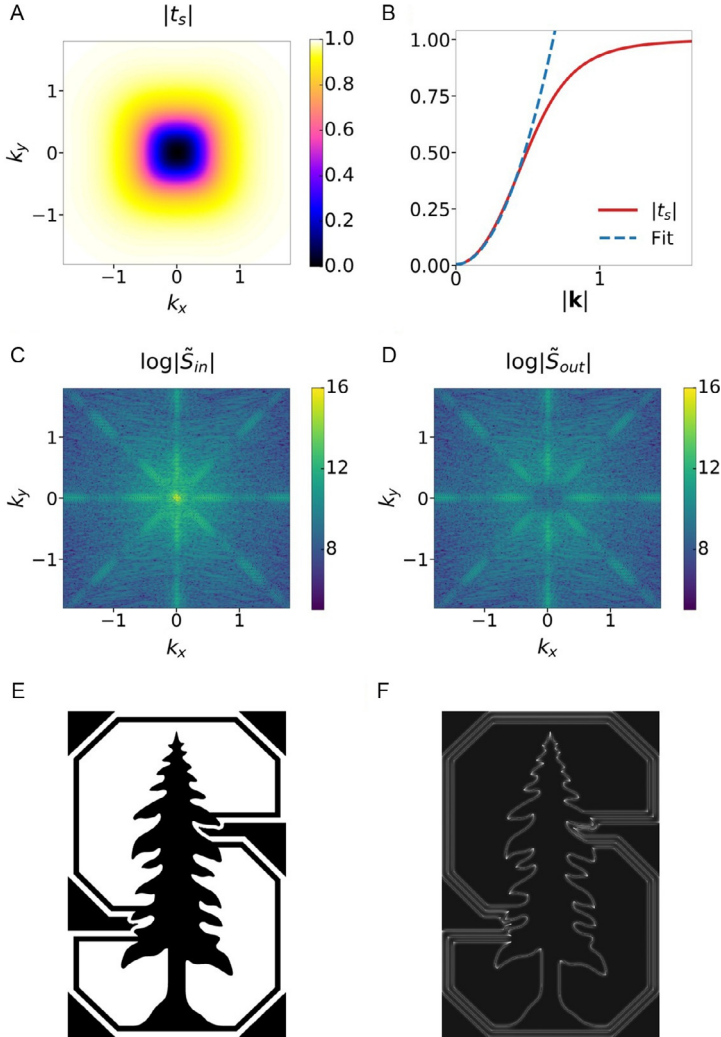
Fig. 4 Isotropic high-pass filter (Laplacian). (A) Transmittance for *S*-polarized light $|t_s|(k_x, k_y)$ at the frequency $\omega_0 = 0.77098 \times 2\pi c/a$. (B) $|t_s|$ as a function of $|\mathbf{k}|$ along a general wavevector direction ($\varphi = 14°$), and the fitting result of Eq. (21). The fit is very good for $|\mathbf{k}|$ up to $0.6 \times 10^{-2} \times 2\pi/a$. (C) Log plot of the Fourier transform of the field profile for the incident image (E): $\log|\tilde{S}_{in}|(k_x, k_y)$. (D) Log plot of the Fourier transform of the field profile for the reflected image (F): $\log|\tilde{S}_{out}|(k_x, k_y)$. The low wavevector components have been filtered out. (E) Incident image $|S_{in}|^2$ of the Stanford emblem. The image size is $5220a \times 3456a$. (F) Calculated transmitted image $|S_{out}|^2$, which shows the edges with different orientations. $|\mathbf{k}|$, k_x, and k_y are in the units of $10^{-2} \times 2\pi/a$. Reprinted with permission from Guo, C., Xiao, M., Minkov, M., Shi, Y., Fan, S., 2018a. Isotropic wavevector domain image filters by a photonic crystal slab device. J. Opt. Soc. Am. A Opt. Image Sci. Vis. 35 (10), 1685–1691, the Optical Society.
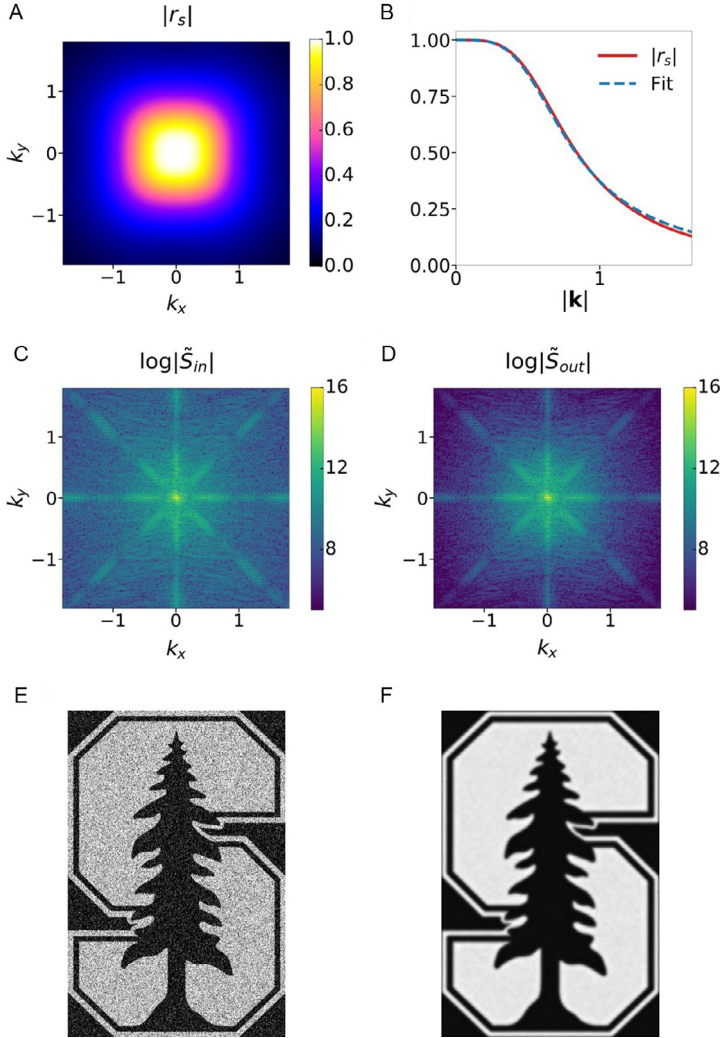
Fig. 5 Isotropic low-pass filter. (A) Reflectance for S-polarized light $|r_s|(k_x, k_y)$ at the frequency $\omega_0 = 0.77098 \times 2\pi c/a$. (B) $|r_s|$ as a function of $|\mathbf{k}|$ along a general wavevector direction ($\varphi = 14°$), and the fitting result of Eq. (22). (C) Log plot of the Fourier transform of the field profile for the incident image (E): $\log|\tilde{S}_{in}|(k_x, k_y)$. (D) Log plot of the Fourier transform of the field profile for the reflected image (F): $\log|\tilde{S}_{out}|(k_x, k_y)$. The high wavevector components have been filtered out. (E) Incident image $|S_{in}|^2$ of the Stanford emblem with substantial white noise component. The image size is $5220a \times 3456a$. (F) Calculated reflected image $|S_{out}|^2$, which reduces the white noise by image smoothing. $|\mathbf{k}|$, k_x, and k_y are in the units of $10^{-2} \times 2\pi/a$. *Reprinted with permission from Guo, C., Xiao, M., Minkov, M., Shi, Y., Fan, S., 2018a. Isotropic wavevector domain image filters by a photonic crystal slab device. J. Opt. Soc. Am. A Opt. Image Sci. Vis. 35 (10), 1685–1691, the Optical Society.*

transform of the field profile for this incident image. Fig. 5D shows the calculated Fourier spectrum for the reflected image, which is obtained by a pointwise product of Fig. 5A and C. The high wavevector components have been filtered out. Fig. 5F shows the calculated reflected image, where the noise component has indeed been significantly reduced, demonstrating image smoothing.

4.3 Isotropic band-reject filter

Fig. 6 illustrates the isotropic band–reject filter. Fig. 6A plots the filter transfer function: the transmittance for S-polarized light $|t_s|(k_x, k_y)$ at the frequency $\omega_q = 0.77130 \times 2\pi c/a$. The transfer function is almost isotropic. Figure 6B plots $|t_s|$ as a function of $|\boldsymbol{k}|$ along a general wavevector direction ($\varphi = 14°$), which shows $|t_s| = 0$ at $|\boldsymbol{k}| = 0.84 \times 10^{-2} \times 2\pi/a$. We fit the transmittance curve with Eq. (23) together with Eq. (12) and $\gamma(\boldsymbol{k}) \approx \gamma_0$. The fitting is almost perfect in the wavevector range as shown. These plots confirm that the device indeed operates as an isotropic band-reject filter in this case.

The isotropic band-reject filter can effectively eliminate periodic noise, a common type of noise arising typically from electrical or electromechanical interference during image acquisition (Aizenberg and Butakoff, 2002; Banham and Katsaggelos, 1997; Gonzalez and Woods, 2008). As periodic noise appears as peaks in the Fourier transform at locations corresponding to the wavevectors of the periodic interference, it can be isolated and filtered by band–reject filters. Here we show an example of periodic noise reduction with the isotropic band-reject filter. Fig. 6E shows an incident image of the Stanford emblem incorporating a periodic noise component. Fig. 6C plots the Fourier transform of the field profile for this incident image. In the wavevector space, the periodic noise appears as spectral peaks which lie on an approximate circle around the origin. Fig. 6D shows the calculated Fourier spectrum for the transmitted image, which is obtained by a pointwise product of Fig. 6A and C. The spectral peaks corresponding to the periodic noise have been filtered out. Fig. 6F shows the calculated transmitted image, where the periodic noise has indeed been eliminated effectively. Here we note that the rejected wavevector where the maximum rejection occurs in our band–reject filter can be easily tuned by tuning the light frequency.

4.4 Isotropic band-pass filter

Fig. 7 illustrates the isotropic band–pass filter. Fig. 7A plots the filter transfer function: the reflectance for S–polarized light $|r_s|(k_x, k_y)$ at the frequency
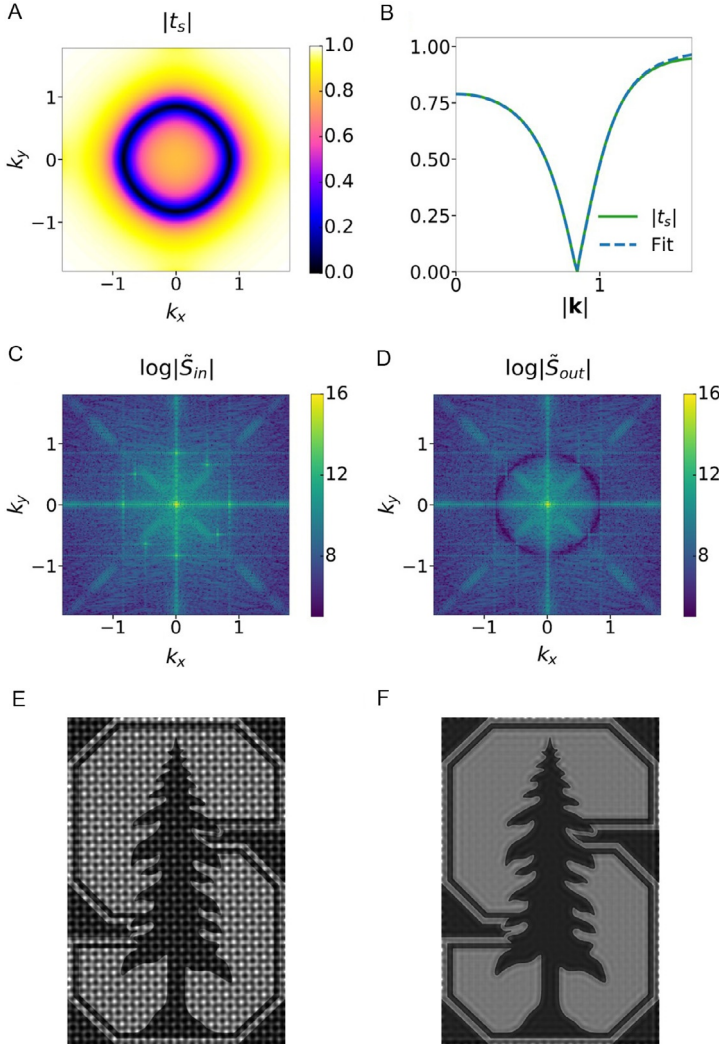
Fig. 6 Isotropic band-reject filter. (A) Transmittance for S-polarized light $|t_s|(k_x, k_y)$ at the frequency $\omega_q = 0.77130 \times 2\pi c/a$. (B) $|t_s|$ as a function of $|\mathbf{k}|$ along a general wavevector direction ($\varphi = 14°$), and the fitting result of Eq. (23) along with Eq. (12) and $\gamma(\mathbf{k}) \approx \gamma_0$. (C) Log plot of the Fourier transform of the field profile for the incident image (E): $\log|\tilde{S}_{in}|(k_x, k_y)$. The sinusoidal noise appears as peaks in the spectrum which lie on an approximate circle around the origin. (D) Log plot of the Fourier transform of the field profile for the transmitted image (F): $\log|\tilde{S}_{out}|(k_x, k_y)$. The wavevector components corresponding to the periodic noise have been filtered out. (E) Incident image $|S_{in}|^2$ of the Stanford emblem with periodic noise. The image size is $5220a \times 3456a$. (F) Calculated transmitted image $|S_{out}|^2$, which eliminates the periodic noise. $|\mathbf{k}|$, k_x, and k_y are in the units of $10^{-2} \times 2\pi/a$. Reprinted with permission from Guo, C., Xiao, M., Minkov, M., Shi, Y., Fan, S., 2018a. Isotropic wavevector domain image filters by a photonic crystal slab device. J. Opt. Soc. Am. A Opt. Image Sci. Vis. 35 (10), 1685–1691, the Optical Society.
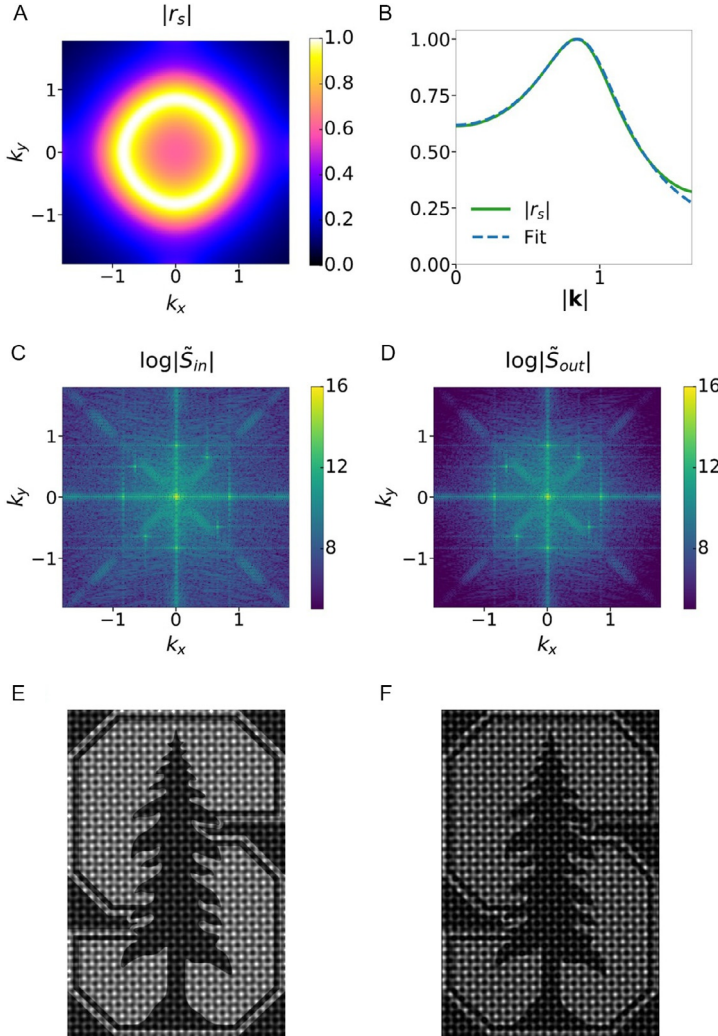
Fig. 7 Isotropic band-pass filter. (A) Reflectance for S-polarized light $|r_s|(k_x, k_y)$ at the frequency $\omega_q = 0.77130 \times 2\pi c/a$. (B) $|r_s|$ as a function of $|\mathbf{k}|$ along a general wavevector direction ($\varphi = 14°$), and the fitting result of Eq. (24) together with Eq. (12) and $\gamma(\mathbf{k}) \approx \gamma_0$. (C) Log plot of the Fourier transform of the field profile for the incident image (E): $\log|\tilde{S}_{in}|(k_x, k_y)$. The sinusoidal noise appears as impulses in the spectrum which lie on an approximate circle around the origin. (D) Log plot of the Fourier transform of the field profile for the reflected image (F): $\log|\tilde{S}_{out}|(k_x, k_y)$. (E) Incident image $|S_{in}|^2$ of the Stanford emblem with periodic noise. The image size is $5220a \times 3456a$. (F) Calculated reflected image $|S_{out}|^2$, which isolates the periodic noise and simplifies its analysis. $|\mathbf{k}|$, k_x, and k_y are in the units of $10^{-2} \times 2\pi/a$. *Reprinted with permission from Guo, C., Xiao, M., Minkov, M., Shi, Y., Fan, S., 2018a. Isotropic wavevector domain image filters by a photonic crystal slab device. J. Opt. Soc. Am. A Opt. Image Sci. Vis. 35 (10), 1685–1691, the Optical Society.*

$\omega_q = 0.77130 \times 2\pi c/a$. The transfer function is almost isotropic. Fig. 7B plots $|r_s|$ as a function of $|\boldsymbol{k}|$ along a general wavevector direction ($\varphi = 14°$), which shows $|r_s| = 1$ at $|\boldsymbol{k}| = 0.84 \times 10^{-2} \times 2\pi/a$. We fit the reflectance curve with Eq. (24) together with Eq. (12) and $\gamma(\boldsymbol{k}) \approx \gamma_0$. The fitting is almost perfect in the wavevector range as shown. These plots confirm that the device indeed operates as an isotropic band-pass filter in this case.

The isotropic band-pass filter performs the opposite operation of the band-reject filter. It is quite useful in isolating the effects on an image caused by selected wavevector bands (Gonzalez and Woods, 2008). Here we show an example of extracting periodic noise patterns with the isotropic band-pass filter. Fig. 7E shows an incident image of the Stanford emblem incorporating periodic noise (same as Fig. 6E), while Fig. 7C plots the Fourier transform of the field profile for this incident image. Fig. 7D shows the calculated Fourier spectrum for the reflected image, which is obtained by a pointwise product of Fig. 7A and C. Fig. 7F shows the calculated reflected image, where the periodic noise pattern is isolated and appears more clearly. This is useful because it simplifies the analysis of the noise, largely independent of the image content (Gonzalez and Woods, 2008).

5. Conclusion

Our design of isotropic wavevector domain image filters using a photonic crystal slab is based on the guided resonances with isotropic band structure. The same idea can extend to other photonic structures that host resonant modes with isotropic band structure. In particular, the phase-shifted Bragg grating in Bykov et al. (2014) can also perform the four filtering functionalities of our device, but with the transmission/reflection mode flipped.

In conclusion, we have shown that isotropic high-pass, low-pass, band-reject, and band-pass filters can be implemented at visible wavelengths using one photonic crystal slab device. Such a simple but multifunctional photonic device may find various applications involving image processing. For instance, it can be used as the first layer of image recognition systems. As such our work indicates the new opportunities for compact, high-throughput, and low-energy-consumption optical analog computing as provided by nanophotonic structures.

References

AbdollahRamezani, S., Arik, K., Khavasi, A., Kavehvash, Z., 2015. Analog computing using graphene-based metalines. Opt. Lett. 40 (22), 5239. ISSN 0146-9592. https://doi.org/10.1364/OL.40.005239. https://www.osapublishing.org/abstract.cfm?URI=ol-40-22-5239.

Abràmoff, M.D., Magalhães, P.J., Ram, S.J., 2004. Image processing with ImageJ. Biophotonics Int. 11 (7), 36–42. ISSN 1081-8693.

Aizenberg, I.N., Butakoff, C., 2002. In: Frequency domain medianlike filter for periodic and quasi-periodic noise removal. Proceedings of SPIE, vol. 4667. San Jose, http://proceedings.spiedigitallibrary.org/proceeding.aspx?articleid=876767. http://link.aip.org/link/?PSI/4667/181/1&Agg=doi.

Banham, M.R., Katsaggelos, A.K., 1997. Digital image restoration. IEEE Signal Process. Mag. 14 (2), 24–41. ISSN 10535888. https://doi.org/10.1109/79.581363. http://ieeexplore.ieee.org/document/581363/.

Bracewell, R.N., 1986. The Fourier Transform and Its Applications. McGraw-Hill, New York. ISBN 0073039381.

Brosnan, T., Sun, D.W., 2004. Improving quality inspection of food products by computer vision—a review. J. Food Eng. 61 (1), 3–16. ISSN 02608774. https://doi.org/10.1016/S0260-8774(03)00183-3.

Buades, A., Coll, B., Morel, J.M., 2005. A review of image denoising algorithms, with a new one. Multiscale Model. Simul. 4 (2), 490–530. ISSN 1540-3459. https://doi.org/10.1137/040616024. http://epubs.siam.org/doi/10.1137/040616024.

Bykov, D.A., Doskolovich, L.L., Bezus, E.A., Soifer, V.A., 2014. Optical computation of the Laplace operator using phase-shifted Bragg grating. Opt. Express 22 (21), 25084. ISSN 1094-4087. https://doi.org/10.1364/OE.22.025084. https://www.osapublishing.org/oe/abstract.cfm?uri=oe-22-21-25084.

Bykov, D.A., Doskolovich, L.L., Morozov, A.A., Podlipnov, V.V., Bezus, E.A., Verma, P., Soifer, V.A., 2018. First-order optical spatial differentiator based on a guided-mode resonant grating. Opt. Express 26 (8), 10997–11006. ISSN 1094-4087. https://doi.org/10.1364/OE.26.010997. https://www.osapublishing.org/abstract.cfm?URI=oe-26-8-10997.

Chang, T.Y., Hong, J.H., Yeh, P., 1990. Spatial amplification: an image-processing technique using the selective amplification of spatial frequencies. Opt. Lett. 15 (13), 743. ISSN 0146-9592. https://doi.org/10.1364/OL.15.000743. https://www.osapublishing.org/abstract.cfm?URI=ol-15-13-743.

Chizari, A., Abdollahramezani, S., Jamali, M.V., Salehi, J.A., 2016. Analog optical computing based on a dielectric meta-reflect array. Opt. Lett. 41 (15), 3451. ISSN 0146-9592. https://doi.org/10.1364/OL.41.003451. https://www.osapublishing.org/abstract.cfm?URI=ol-41-15-3451. https://arxiv.org/abs/1605.07150%0Ahttp://doi.org/10.1364/OL.41.003451.

Dalal, N., Triggs, B., 2005. Histograms of oriented gradients for human detection. In: 2005 IEEE Computer Society Conference on Computer Vision and Pattern Recognition (CVPR'05) IEEE, pp. 886–893.

Dong, Z., Si, J., Yu, X., Deng, X., 2018. Optical spatial differentiator based on subwavelength high-contrast gratings. Appl. Phys. Lett. 112 (18), 181102. ISSN 0003–6951. https://doi.org/10.1063/1.5026309. http://aip.scitation.org/toc/apl/112/18. http://aip.scitation.org/doi/10.1063/1.5026309. https://doi.org/10.1063/1.5026309.

Eu, J.K.T., Liu, C.Y.C., Lohmann, A.W., 1973. Spatial filters for differentiation. Opt. Commun. 9 (2), 168–171. ISSN 00304018. https://doi.org/10.1016/0030-4018(73)90251-4. http://linkinghub.elsevier.com/retrieve/pii/0030401873902514.

Fan, S., Joannopoulos, J.D., 2002. Analysis of guided resonances in photonic crystal slabs. Phys. Rev. B 65 (23), 235112. ISSN 0163-1829. https://doi.org/10.1103/PhysRevB.65.235112.

Fang, Y., Ruan, Z., 2018. Optical spatial differentiator for a synthetic three-dimensional optical field. Opt. Lett. 43 (23), 5893–5896.

Fang, Y., Lou, Y., Ruan, Z., 2017. On-grating graphene surface plasmons enabling spatial differentiation in the terahertz region. Opt. Lett. 42 (19), 3840. ISSN 0146-9592. https://doi.org/10.1364/OL.42.003840. https://www.osapublishing.org/abstract.cfm?URI=ol-42-19-3840.

Golovastikov, N.V., Bykov, D.A., Doskolovich, L.L., 2014. Resonant diffraction gratings for spatial differentiation of optical beams. Quantum Electron. 44 (10), 984–988. ISSN 1063-7818. https://doi.org/10.1070/QE2014v044n10ABEH015477. http://stacks.iop.org/1063-7818/44/i=10/a=984?key=crossref.8bee7b769ad2412f3500ff65fffe3a5e%5Cn. http://iopscience.iop.org/1063-7818/44/10/984. http://stacks.iop.org/1063-7818/44/i=10/a=984?key=crossref.8bee7b769ad2412f3500ff65fffe3a5e.

Gonzalez, R., Woods, R., 2008. Digital Image Processing, third ed. Prentice Hall, Upper Saddle River, NJ. ISBN 9780131687288.

Goodman, J.W., 2005. Introduction to Fourier Optics, third ed. Roberts and Company, Englewood. ISBN 0974707724.

Görlitz, D., Lanzl, F., 1975. A holographic spatial filter for direction independent differentiation. Jpn. J. Appl. Phys. 14 (S1), 223. ISSN 0021-4922. https://doi.org/10.7567/JJAPS.14S1.223. http://stacks.iop.org/1347-4065/14/223.

Guo, C., Xiao, M., Minkov, M., Shi, Y., Fan, S., 2018a. Isotropic wavevector domain image filters by a photonic crystal slab device. J. Opt. Soc. Am. A Opt. Image Sci. Vis. 35 (10), 1685–1691.

Guo, C., Xiao, M., Minkov, M., Shi, Y., Fan, S., 2018b. Photonic crystal slab Laplace operator for image differentiation. Optica 5 (3), 251. ISSN 2334-2536. https://doi.org/10.1364/OPTICA.5.000251. https://www.osapublishing.org/abstract.cfm?URI=optica-5-3-251.

Hwang, Y., Davis, T.J., Lin, J., Yuan, X.C., 2018. Plasmonic circuit for second-order spatial differentiation at the subwavelength scale. Opt. Express 26 (6), 7368. ISSN 1094-4087. https://doi.org/10.1364/OE.26.007368. https://www.osapublishing.org/abstract.cfm?URI=oe-26-6-7368.

Kwon, H., Sounas, D., Cordaro, A., Polman, A., Alù, A., 2018. Nonlocal metasurfaces for optical signal processing. Phys. Rev. Lett. 121 (17), 173004.

Markham, R., Frey, S., Hills, G.J., 1963. Methods for the enhancement of image detail and accentuation of structure in electron microscopy. Virology 20 (1), 88–102. ISSN 00426822. https://doi.org/10.1016/0042-6822(63)90143-0. http://linkinghub.elsevier.com/retrieve/pii/0042682263901430.

Nejad, F.Z., Fleury, R., 2018. Performing mathematical operations using high–index acoustic metamaterials. New J. Phys. 20, 073001.

Ochiai, T., Sakoda, K., 2001. Dispersion relation and optical transmittance of a hexagonal photonic crystal slab. Phys. Rev. B 63 (12), 125107. ISSN 0163-1829. https://doi.org/10.1103/PhysRevB.63.125107.

Pors, A., Nielsen, M.G., Bozhevolnyi, S.I., 2015. Analog computing using reflective plasmonic metasurfaces. Nano Lett. 15 (1), 791–797. ISSN 1530-6984. https://doi.org/10.1021/nl5047297.

Roberts, A., Gómez, D.E., Davis, T.J., 2018. Optical image processing with metasurface dark modes. J. Opt. Soc. Am. A Opt. Image Sci. Vis. 35 (9), 1575–1584.

Sakoda, K., 2005. Optical properties of photonic crystals, Springer Series in Optical Sciences, vol. 80. Springer-Verlag, Berlin, Heidelberg. ISBN 3-540-20682-5.

Silva, A., Monticone, F., Castaldi, G., Galdi, V., Alu, A., Engheta, N., 2014. Performing mathematical operations with metamaterials. Science. 343 (6167), 160–163. ISSN 0036-8075. https://doi.org/10.1126/science.1242818.

Sirohi, R.S., Mohan, V.R., 1977. Differentiation by spatial filtering. Opt. Acta 24 (11), 1105–1113. ISSN 0030-3909. https://doi.org/10.1080/713819447. http://www.tandfonline.com/doi/abs/10.1080/713819447.

Solli, D.R., Jalali, B., 2015. Analog optical computing. Nat. Photonics 9 (11), 704–706. ISSN 1749-4885. https://doi.org/10.1038/nphoton.2015.208. http://www.nature.com/doifinder/10.1038/nphoton.2015.208.

Tikhodeev, S.G., Yablonskii, A.L., Muljarov, E.A., Gippius, N.A., Ishihara, T., 2002. Quasiguided modes and optical properties of photonic crystal slabs. Phys. Rev. B 66 (4), 045102. ISSN 0163-1829. https://doi.org/10.1103/PhysRevB.66.045102.

Vogelaar, L., Nijdam, W., van Wolferen, H.A.G.M., de Ridder, R.M., Segerink, F.B., Flück, E., Kuipers, L., van Hulst, N.F., 2001. Large area photonic crystal slabs for visible light with waveguiding defect structures: fabrication with focused ion beam assisted laser interference lithography. Adv. Mater. 13 (20), 1551. ISSN 09359648. https://doi.org/10.1002/1521-4095(200110)13:20¡1551::AID-ADMA1551¿3.0.CO;2-V. http://doi.wiley.com/10.1002/1521-4095%28200110%2913%3A20%3C1551%3A%3AAID-ADMA1551%3E3.0.CO%3B2-V.

Wang, K.X., Yu, Z., Sandhu, S., Fan, S., 2013. Fundamental bounds on decay rates in asymmetric single-mode optical resonators. Opt. Lett. 38 (2), 100. ISSN 0146-9592. https://doi.org/10.1364/OL.38.000100. https://www.osapublishing.org/abstract.cfm?URI=ol-38-2-100.

Wu, W., Jiang, W., Yang, J., Gong, S., Ma, Y., 2017. Multilayered analog optical differentiating device: performance analysis on structural parameters. Opt. Lett. 42 (24), 5270. ISSN 0146-9592. https://doi.org/10.1364/OL.42.005270. https://www.osapublishing.org/abstract.cfm?URI=ol-42-24-5270.

Youssefi, A., Zangeneh-Nejad, F., Abdollahramezani, S., Khavasi, A., 2016. Analog computing by Brewster effect. Opt. Lett. 41 (15), 3467. ISSN 0146-9592. https://doi.org/10.1364/OL.41.003467. https://www.osapublishing.org/abstract.cfm?URI=ol-41-15-3467.

Yu, F.T.S., Jutamulia, S., Yin, S., 2001. Introduction to Information Optics. Academic Press, San Diego. ISBN 0127748113.

Zhou, W., Zhao, D., Shuai, Y.C., Yang, H., Chuwongin, S., Chadha, A., Seo, J.H., Wang, K.X., Liu, V., Ma, Z., Fan, S., 2014. Progress in 2D photonic crystal Fano resonance photonics. Prog. Quantum Electron. 38 (1), 1–74. ISSN 00796727. https://doi.org/10.1016/j.pquantelec.2014.01.001. http://linkinghub.elsevier.com/retrieve/pii/S0079672714000020. https://doi.org/10.1016/j.pquantelec.2014.01.001.

Zhu, T., Zhou, Y., Lou, Y., Ye, H., Qiu, M., Ruan, Z., Fan, S., 2017. Plasmonic computing of spatial differentiation. Nat. Commun. 8, 15391. ISSN 2041-1723. https://doi.org/10.1038/ncomms15391. http://www.nature.com/doifinder/10.1038/ncomms15391. https://doi.org/10.1038/ncomms15391.